Biomedical Signal Processing and Control 67 (2021) 102560

Contents lists available at ScienceDirect

Biomedical Signal Processing and Control

journal homepage: www.elsevier.com/locate/bspc

A method to improve the computational efficiency of the Chan-Vese model for the segmentation of ultrasound images

Saru Meena Ramu [a], Muthaiah Rajappa [a,*], Kannan Krithivasan [b], Jaikanth Jayakumar [a], Panagiotis Chatzistergos [c], Nachiappan Chockalingam [c]

[a] SASTRA Deemed University, School of Computing, Thanjavur, India
[b] SASTRA Deemed University, School of Education, Thanjavur, India
[c] Staffordshire University, Centre for Biomechanics and Rehabilitation Technologies, Stoke-on-Trent, United Kingdom

ARTICLE INFO

Keywords:
Ultrasonography
Image segmentation
Deformable model
Variational approach
Chan–Vese model
Musculoskeletal

ABSTRACT

Purpose: Advanced image segmentation techniques like the Chan-Vese (CV) models transform the segmentation problem into a minimization problem which is then solved using the gradient descent (GD) optimization algorithm. This study explores whether the computational efficiency of CV can be improved when GD is replaced by a different optimization method.

Methods: Two GD variants from the literature (Nesterov accelerated, Barzilai-Borwein) and a newly developed hybrid variant of GD were used to improve the computational efficiency of CV by making GD insensitive to local minima. One more variant of GD from the literature (projected GD) was used to address the issue of maintaining the constraint on boundary evolution in CV which also increases computational cost. A novel modified projected GD (Barzilai-Borwein projected GD) was also used to overcome both problems at the same time. The effect of optimization method selection on processing time and the quality of the output was assessed for 25 musculoskeletal ultrasound images (five anatomical areas).

Results: The Barzilai-Borwein projected GD method was able to significantly reduce computational time (average (±std.dev.) reduction 95.82 % (±3.60 %)) with the least structural distortion in the delineated output relative to the conventional GD (average(±std.dev.) structural similarity index: 0.91(±0.06)).

Conclusion: The use of an appropriate optimization method can substantially improve the computational efficiency of CV models. This can open the way for real-time delimitation of anatomical structures to aid the interpretation of clinical ultrasound. Further research on the effect of the optimization method on the accuracy of segmentation is needed.

1. Introduction

Ultrasound (US) imaging is widely used in clinics around the world due to its high availability, non-invasive nature, and capacity for bedside monitoring of patients. However, US imaging remains operator-dependent and compared to other medical imaging modalities, the quality of the produced images is relatively low which can make their interpretation challenging.

Computerized delineation algorithms based on deformable models are well suited for the analysis of US images [1,2] because of their flexibility and their ability to perform delineation with the use of constraints (derived from image data) together with the prior knowledge of the shape, location or size of the targeted structures. Moreover, these models can better accommodate the shape variability of biological structures across individuals and they are robust to noise and boundary gaps because of the constraints imposed. The key idea of deformable model based segmentation is that a prior model of the structure of interest is represented either as a 2D curve or as a 3D surface in the image domain and this curve or surface undergoes deformation in an iterative manner to fit onto the boundary of the structure of interest. The deformation field that tells how the model should deform to fit onto the boundary of the structure of interest is obtained by the minimization of an energy functional. Therefore, the segmentation problem is now transformed into an energy functional minimization problem which can be solved with the help of an optimization algorithm [3,4].

This study will focus on one of the most representative and widely

* Corresponding author.
E-mail address: muthaiah66@gmail.com (M. Rajappa).

https://doi.org/10.1016/j.bspc.2021.102560
Received 24 October 2020; Received in revised form 18 February 2021; Accepted 7 March 2021

used deformable models called Chan–Vese (CV) model [5,6]. The CV model is a piecewise constant approximation of a global region information based deformable model called Mumford–Shah (MS) model [5, 6].The CV model assumes that each region is homogenous with respect to grayscale intensities within a region and it uses the mean of grayscale intensities within a region as a region descriptor to generate a force that pulls the shape model (represented by level set) towards the organ of interest. At the end, CV partitions the image into distinct non-overlapping regions with just two levels of intensity: m_1 and m_2 where m_1 is the mean of grayscale intensities inside the contour and m_2 is the mean of grayscale intensities outside the contour [7].

The CV model is topologically flexible, less sensitive to noise and the initial position of the shape model and can segment structures with weak boundaries. However, one of the key limitations of the CV model is its high computational cost [5,6,8–10]. The causes of the computational inefficiency of the CV model are: a) the use of the gradient descent (GD) optimization technique to solve the non-convex optimization problem of CV and b) the need to use numerical remedies to maintain the constraint on level set function (LSF) during contour evolution [5,11,12]. In the literature, the numerical difficulties related to solving the non-convex optimization problem with GD (i.e. convergence towards local optimum and slow convergence towards optimum) were addressed either by using a convex relaxation approach or by using advanced alternatives to GD (second order optimization methods, subdivision schemes, stochastic optimization schemes) or by modifying the gradient descent search direction [12–15].

According to the convex relaxation approach, an energy functional that is non-convex in nature is transformed into an energy functional that is convex in nature by relaxing the constraint so that the resulting convex energy functional could be easily solved by using convex optimization schemes such as the split Bregman method. The split Bregman technique is a constrained optimization scheme that is suitable for faster minimization of a convex energy functional [13,14,16–18]. Even though the convex relaxation approach makes numerical implementation easier, this comes at the cost of compromised segmentation accuracy [13,14].

On the contrary, advanced alternatives of GD, such as subdivision schemes, could maintain the segmentation accuracy but they are highly complex in nature and as a result they are mainly limited to solving small problems. Similarly stochastic optimization techniques are logarithmically slow which also restricts their applicability [12]. Second order optimization methods, such as the Newton Raphson method, lead to faster convergence towards optimum. However, the limitation of Newton Raphson (Newtonian search direction) method is the need for the Hessian (second order derivative matrix) computation at each iteration. Explicit computation of matrix of second order derivatives can sometimes be a cumbersome, error-prone, and computationally expensive process [19].

Modifying the search direction in GD can improve the performance of GD when used to solve non-convex optimization problems while avoiding the complexity of more advanced optimization techniques with no compromise in segmentation accuracy (i.e. without making any changes in the original non-convex energy functional) [12]. Methods that modify the search direction in GD provide GD with the "intelligence" to escape local minima and ravines by using mathematical entities to adapt the search direction thereby leading to faster convergence towards an optimum solution [12]. Inspired from the key idea presented in Andersson et.al.(2013) [12], three variants of GD are proposed in the present study, which differ in the way they modify the search direction in GD. The first proposed variant of GD uses a smart momentum term to modify the search direction in GD. This proposed smart momentum term based GD is different from the ordinary momentum based GD in the sense that the new smart momentum term helps GD to escape local minima and ravine but at the same time, it wouldn't make GD to run past the optimum solution (i.e.) GD will stop when the optimum is reached. This smart momentum based GD is called Nesterov accelerated gradient descent (NA-GD). This variant of GD is commonly used in machine learning applications for the updation of weights in neural networks. The second proposed variant of GD is called Barzilai and Borwein gradient descent method (BB-GD) and it is based on the idea of using a step size that enforces quasi-Newton property along with the negative direction of gradient [20–22]. The third proposed variant of GD is a novel modified NA-GD (hybrid method). This newly developed hybrid method is based on the idea of replacing the fixed step size in NA-GD with the step size formulation of BB-GD method so that the computational efficiency of NA-GD could be improved.

As previously mentioned, the second factor that interferes with the computational efficiency of the CV model is the requirement to maintain a specific constraint on LSF during contour evolution. More specifically, with the level set modelling of evolving boundaries in CV, it is necessary to maintain the LSF as a signed distance function (SDF) during contour evolution to avoid numerical errors and to preserve the stability of level set evolution [11,23–25]. In the literature, this constraint on LSF was maintained either by using a periodic re-initialization process or by adding a quadratic penalty term with the constraint to be enforced in the energy functional (penalty term approach) [11,24,26]. However, periodic re-initialization is a time-consuming process and it may move the zero level set away from the desired position [11,24]. At the same time, enforcing the constraint through a penalty term approach may cause undesirable side effects on the LSF which would in turn affect numerical accuracy [11,24]. This is because, the penalty term approach cannot guarantee that LSF will be maintained as SDF during contour evolution. More specifically, the weighting parameter associated with the quadratic penalty term should be sufficiently large to enforce the constraint while the step size in GD should be chosen to be sufficiently small to maintain the Courant–Friedrichs–Lewy (CFL) stability condition [11]. However, the use of smaller step size in GD can significantly compromise the computational efficiency of the segmentation process. Therefore, these numerical remedies for maintaining the constraint on LSF end up being computationally intensive by themselves which in turn increases the computational cost of the CV model.

An alternative way to solve the energy functional with a quadratic penalty term without violating the CFL condition was presented by Duan et al. (2014) [11]. According to their approach, a projection concept was applied to a subdivision scheme called augmented Lagrangian. Even though this approach does not solve the inherent problems of computational efficiency associated with the use of GD, the concept of projection appears to offer a noncomplex solution to maintain the constrain of LSF.

Inspired from the idea of projection [11], we are proposing to use a first order constrained optimization scheme called projected gradient descent (PGD) to maintain the constraint on LSF during contour evolution. In this case, the unconstrained non-convex optimization problem of the CV model is posed as a constrained non-convex optimization problem and solved using PGD to find an optimum solution. The basic idea of PGD is that at each iteration, the solution is computed by traversing in the negative direction of the gradient and projecting the obtained solution onto the constraint set $\mathbb{C}$ [27]. In the present work, the constraint set $\mathbb{C}$ is formed by a set of all LSF's (φ) that satisfy the constraint $|\nabla\varphi| = 1$, which is non-convex in nature. PGD indirectly forces the LSF to remain close to SDF with the help of the projection onto non-convex constraint set $\mathbb{C}$ thereby maintaining the constraint on LSF during contour evolution. PGD is the fourth variant of GD that will be tested in the present study.

However, since PGD is just GD used to solve a constrained optimization problem, the numerical difficulties related to solving a non-convex optimization problem with GD remain for PGD too. Therefore, the fifth and the final variant of GD is proposed based on the idea of using a step size that enforces quasi newton property within PGD formulation. This accelerated version of PGD, called Barzilai and Borwein projected gradient descent (BB-PGD), has the twofold advantage of maintaining the constraint on LSF during contour evolution in a smart

manner while helping GD to escape local minima and ravine [28].

2. Materials and methods

2.1. CV models

Two different versions of the CV model were included in this study: the conventional CV model [5,7] and its speckle noise handling modification called modified Chan-Vese (MCV) model [29,30]. The energy functional of CV model and MCV model is given in Eqs. (1) and (2) respectively.

$$E^{CV}(m_1,m_2,\Gamma) = \rho.Length\ (\Gamma) + \gamma.\ area\ (in\ (\Gamma)) + \beta_1 \int_{\Omega_1} (z-m_1)^2 dx\,dy + \beta_2 \int_{\Omega_2} (z-m_2)^2 dx\,dy \tag{1}$$

where z is the input image; Γ is the deformable boundary curve; $in\ (\Gamma)$ is inside the boundary curve; Ω_1 is the image region within the contour and Ω_2 is the image region outside the contour. The first two terms in the energy functional denote the regularizer terms; the third and the fourth terms denote the data fidelity terms. $\beta_1 and\ \beta_2$ are the weighing constant associated with the two data fidelity terms while ρ and γ are the weighting constants associated with the arc length term and the area constraint term respectively.

The CV model implicitly assumes that the input image is perturbed by additive noise which is modelled by zero mean Gaussian probability density function (PDF).When this model is used to segment US images, it can produce sub-optimum results since US images are corrupted by speckle noise which is multiplicative in nature and it is modelled by non-Gaussian PDF [29–32]. In the literature, this problem was addressed by introducing physical noise modelling within the segmentation paradigm of the CV model through Bayesian modelling [29,33,34].With the displayed US image being modelled by Loupas noise model, the energy functional of MCV model is given by (2).

$$E^{MCV}(m_1,m_2,\Gamma) = \rho.Length\ (\Gamma) + \gamma.\ area\ (in\ (\Gamma)) + \beta_1 \int_{\Omega_1} \frac{(z-m_1)^2}{m_1} dx\,dy + \beta_2 \int_{\Omega_2} \frac{(z-m_2)^2}{m_2} dx\,dy \tag{2}$$

In CV and MCV models, the deformable curve is represented implicitly as a zero level set of a higher dimensional surface called LSF. The idea of level set method is to evolve the higher dimensional surface instead of evolving the curve. The LSF used is the SDF. An alternative representation of interface is through a regularized Heaviside function. The energy functional of CV and MCV models in level set framework is given by (3) and (4) respectively.

$$E^{CVLS}(m_1,m_2,\varphi) = \rho \int_{\Omega} \delta_\varepsilon(\varphi)|\nabla\varphi|\ dx\,dy + \beta_1 \int_{\Omega_1} (z-m_1)^2 H_\varepsilon(\varphi)\ dx\,dy + \beta_2 \int_{\Omega_2} (z-m_2)^2 (1-H_\varepsilon(\varphi))\ dx\,dy \tag{3}$$

$$E^{MCVLS}(m_1,m_2,\varphi) = \rho \int_{\Omega} \delta_\varepsilon(\varphi)|\nabla\varphi|\ dx\,dy + \beta_1 \int_{\Omega_1} \frac{(z-m_1)^2}{m_1} H_\varepsilon(\varphi)\ dx\,dy + \beta_2 \int_{\Omega_2} \frac{(z-m_2)^2}{m_2} (1-H_\varepsilon(\varphi))\ dx\,dy \tag{4}$$

where φ is the LSF; $H_\varepsilon(\varphi)$ is the regularized Heaviside function; $\delta_\varepsilon(\varphi)$ is the derivative of regularized Heaviside function.

The level set evolution equation of CV model is given by (5).

$$\frac{\partial\varphi}{\partial t} = -\frac{\partial E^{CVLS}}{\partial\varphi} \tag{5a}$$

$$\frac{\partial E^{CVLS}}{\partial\varphi} = \delta_\varepsilon(\varphi)\left[-\rho\ div\left(\frac{\nabla\varphi}{|\nabla\varphi|}\right) + \beta_1(z-m_1)^2 - \beta_2\ (z-m_2)^2\right] \tag{5b}$$

$$\frac{\partial\varphi}{\partial t} = \delta_\varepsilon(\varphi)\left[\rho\ div\left(\frac{\nabla\varphi}{|\nabla\varphi|}\right) - \beta_1(z-m_1)^2 + \beta_2\ (z-m_2)^2\right] \tag{5c}$$

To solve $\frac{\partial\varphi}{\partial t}$ in (5a) numerically, $\frac{\partial\varphi}{\partial t}$ is discretized using finite difference implicit scheme and the level set updation equation for CV model is given by (6).

$$\varphi^{k+1} = \varphi^k - \xi\ \frac{\partial E^{CVLS}}{\partial\varphi} \tag{6a}$$

$$\varphi^{k+1} = \varphi^k + \xi\ \frac{\partial\varphi^k}{\partial t} \tag{6b}$$

The level set evolution equation of MCV model is given by (7).

$$\frac{\partial\varphi}{\partial t} = -\frac{\partial E^{MCVLS}}{\partial\varphi} \tag{7a}$$

$$\frac{\partial E^{MCVLS}}{\partial\varphi} = \delta_\varepsilon(\varphi)\left[-\rho\ div\left(\frac{\nabla\varphi}{|\nabla\varphi|}\right) + \beta_1\ \frac{(z-m_1)^2}{m_1} - \beta_2\ \frac{(z-m_2)^2}{m_2}\right] \tag{7b}$$

$$\frac{\partial\varphi}{\partial t} = \delta_\varepsilon(\varphi)\left[\rho\ div\left(\frac{\nabla\varphi}{|\nabla\varphi|}\right) - \beta_1\ \frac{(z-m_1)^2}{m_1} + \beta_2\ \frac{(z-m_2)^2}{m_2}\right] \tag{7c}$$

To solve $\frac{\partial\varphi}{\partial t}$ in (7a) numerically, $\frac{\partial\varphi}{\partial t}$ is discretized using finite difference implicit scheme and the level set updation equation for MCV model is given by (8).

$$\varphi^{k+1} = \varphi^k - \xi\ \frac{\partial E^{MCVLS}}{\partial\varphi} \tag{8a}$$

$$\varphi^{k+1} = \varphi^k + \xi\ \frac{\partial\varphi^k}{\partial t} \tag{8b}$$

where k is the iteration index; φ^{k+1} is the value of φ at next step; φ^k is the value of φ at current step and ξ is the step size that decides how fast the solution converges towards optimum. (6b) and (8b) can be interpreted as: the shape model represented (via.) initial level set is deformed in the negative direction of the gradient to fit it onto the closed boundary of the structure of interest. The solution to the image processing problem (segmentation in this case) is obtained by solving (6b) and (8b) to steady state [7–9,29,30].

The detailed mathematical formulation of the conventional CV and MCV models can be found in Supplementary material A.

2.2. Optimization methods

Since the energy functional of both the CV and MCV models are non-convex in nature, the use of GD would lead to problems such as convergence towards local minima and slow convergence towards the global optimum due to its inability to come out of pathological curvature areas called ravines when trapped into it [5,8,12,35,36].

This limitation of GD has been addressed in literature by using mathematical entities that can change the search direction in GD to escape local minima and ravines. This approach can lead to faster convergence towards the optimum solution while avoiding the complexity of more advanced optimization techniques and with no compromise in segmentation accuracy (i.e. without making any changes in the original non-convex energy functional) [12,37]. In this context,

three variants of GD are used in the present study, which differ in the way the search direction in GD is modified [20–22].

- **Nesterov accelerated GD (NA-GD):** This method uses a smart momentum term to modify the search direction in GD which avoids getting trapped in local minima and ravines but at the same time also avoids running past the optimum solution [20,22]. The level set evolution equation of the NA-GD method is given by (9).

$$\varphi^{k+1} = \nu^k - \xi \nabla f(\nu^k) \tag{9a}$$

$$\text{where } \nu^k = \varphi^k + \left(\frac{k-1}{k+2}\right)\left[\varphi^k - \varphi^{k-1}\right] \tag{9b}$$

- **Barzilai and Borwein GD (BB-GD):** This method improves the efficiency of GD by changing the way that the step size is calculated in the search for global optimum [21]. The level set evolution equation of the BB-GD method is given by (10).

$$\varphi^{k+1} = \varphi^k - \xi \frac{\partial E^{MCVLS}}{\partial \phi} \tag{10a}$$

$$\text{where } \xi = \frac{\nu'^k}{\nu''^k} \tag{10b}$$

$$\nu'^k = \varphi^{k+1} - \varphi^k;\ \nu''^k = \left(\frac{\partial E^{MCVLS}}{\partial \phi}\right)^{k+1} - \left(\frac{\partial E^{MCVLS}}{\partial \phi}\right)^{k} \tag{10c}$$

- **Hybrid method (Hybrid):** The fixed step size in NA-GD is replaced by the step size formulation in BB-GD. The level set evolution equation of the hybrid method is given by (11).

$$\varphi^{k+1} = \nu^k - \xi \nabla f(\nu^k) \tag{11a}$$

$$\text{where } \nu^k = \varphi^k + \left(\frac{k-1}{k+2}\right)\left[\varphi^k - \varphi^{k-1}\right] \tag{11b}$$

$$\xi = \frac{\nu'^k}{\nu''^k};\nu'^k = \varphi^{k+1} - \varphi^k; \nu''^k = \left(\frac{\partial E^{MCVLS}}{\partial \phi}\right)^{k+1} - \left(\frac{\partial E^{MCVLS}}{\partial \phi}\right)^{k} \tag{11c}$$

One additional first order constrained optimization scheme was used to address the limitation associated with level set modelling of evolving boundaries (increased computational complexity) in the CV model and MCV model:

- **Projected GD (PGD):** The basic idea of PGD is that at each iteration, the algorithm computes the solution by traversing in the negative direction of the gradient and project the obtained solution onto the constraint set $\mathbb{C}$ [27]. In our work, the constraint set $\mathbb{C}$ is formed by set of all φ's that satisfy the constraint $|\nabla\varphi| = 1$ and this constraint set is non-convex in nature. PGD indirectly forces the LSF to remain close to SDF (via.) the projection onto non-convex constraint set $\mathbb{C}$ thereby maintaining the constraint on LSF during contour evolution in a smart manner. The constrained non-convex optimization problem to be solved by using PGD is given in (12).

$$\begin{aligned} E^{MCVLS}(m_1, m_2, \varphi) = {} & \rho \int_{\Omega} \delta_\varepsilon(\varphi)\, |\nabla\varphi|\, dx\, dy + \beta_1 \int_{\Omega_1} \frac{(z-m_1)^2}{m_1} H_\varepsilon(\varphi)\, dx\, dy \\ & + \beta_2 \int_{\Omega_2} \frac{(z-m_2)^2}{m_2} (1 - H_\varepsilon(\varphi))\, dx\, dy \quad \text{s.t. } |\nabla\varphi| \\ = {} & 1 \end{aligned} \tag{12}$$

Generally, the projection of a point q onto set L is given by (13)

$$\Pi_L(q) = \min_{l \in L} \frac{1}{2} \|l - q\|_2^2 \tag{13}$$

Level set updation equation using PGD is given by (14) and (15)

$$\varphi^{k+1} = \Pi_{\mathbb{C}}\, \breve{\varphi}^{k+1} \tag{14}$$

$$where\ \breve{\varphi}^{k+1} = \varphi^k - \xi \frac{\partial E^{MCVLS}}{\partial \varphi} \tag{15}$$

However, since PGD is just GD used to solve a constrained optimization problem, the numerical difficulties related to solving a non-convex optimization problem with GD remain in PGD too. Therefore, to improve the efficiency of PGD, an accelerated version of PGD that uses the step size of BB-GD within the PGD formulation (BB-PGD) has been developed [28].

- **Barzilai-Borwein projected gradient descent (BB-PGD):** BB-PGD has a twofold advantage of maintaining the constraint on LSF during contour evolution in a smart manner while helping GD to escape local minima and ravines. The constrained non-convex optimization problem to be solved by BB-PGD is given in (12) and its level set evolution by (16).

$$\varphi^{k+1} = \Pi_{\mathbb{C}}\, \breve{\varphi}^{k+1} \tag{16a}$$

$$\text{where } \breve{\varphi}^{k+1} = \varphi^k - \xi \frac{\partial E^{MCVLS}}{\partial \phi} \text{ and } \xi = \frac{\nu'^k}{\nu''^k} \tag{16b}$$

$$\nu'^k = \varphi^{k+1} - \varphi^k\ ;\nu''^k = \left(\frac{\partial E^{MCVLS}}{\partial \phi}\right)^{k+1} - \left(\frac{\partial E^{MCVLS}}{\partial \phi}\right)^{k} \tag{16c}$$

The sequence of steps in solving an energy functional minimization problem with the proposed variants of GD is as follows:

Input: US image, maximum number of iterations N and step size ξ
Models used: Conventional CV model and MCV model
Output: Segmented image

- Define an initial contour as scaled versions of circle within the image domain.
- Calculate the stopping criterion threshold ζ using the relation $\zeta = \xi \times (0.18)^2$.

for $k = 1, 2, \ldots\ldots N$

- Compute m_1 *and* m_2 where m_1 is mean of gray levels inside the contour and m_2 is the mean of gray levels outside the contour.
- Evolve the level set using GD and proposed variants of GD.
- Compute $d = \left|\varphi^{k+1} - \varphi^k\right|$
- **Convergence criterion:** Check if $d \le \zeta$. Goto to next step if "no". Stop the evolution process if "yes".
- Check if the iteration index k is less than or equal to maximum number of iterations N. Proceed with the evolution process if "yes". Stop the evolution process if "no".

The efficiency of individual optimisation methods is demonstrated by their order of convergence in terms of iteration complexity for GD and the proposed variants of GD (Table 1).

2.3. Case study

The purpose of this case study was to assess whether the use of the alternative first order optimization methods could improve the computational efficiency of the CV or MCV models. The software platform used was MATLAB ® 2017b (Mathworks Inc., Natick, MA, USA) and all the experiments were performed using a computer system with i5 core @1.8 GHz and 8 GB RAM.

Table 1
Order of convergence for GD and the proposed variants of GD.

S. No.	Optimization technique	Iteration complexity
1	GD	$\mathcal{O}\left(\frac{1}{\zeta}\right)$ [20]
2	NA-GD	$\mathcal{O}\left(\frac{1}{\sqrt{\zeta}}\right)$ [20]
3	BB-GD	$\mathcal{O}\left(\log\left(\log\frac{1}{\zeta}\right)\right)$ [38]
4	Hybrid	$\mathcal{O}\left(\log\left(\log\frac{1}{\zeta}\right)\right)$
5	PGD	For a non-convex function satisfying $\mathscr{A}$ restricted strong convexity and $\mathscr{B}$ restricted smoothness over a non-convex constraint set with $\frac{\mathscr{B}}{\mathscr{A}} < 2$, the optimum will be obtained after $\mathcal{O}\left(\frac{\mathscr{A}}{2\mathscr{A}-\mathscr{B}}\log\left(\frac{1}{\zeta}\right)\right)$ iterations, which is much less than number of iterations required to obtain the optimum in GD ($\mathcal{O}\left(\frac{1}{\zeta}\right)$) [27]
6	BB-PGD	$\mathcal{O}\left(\log\left(\log\frac{1}{\zeta}\right)\right)$

In this study, two tendons (Achilles tendon and patellar tendon) were imaged in five healthy adults thereby producing ten images. Three muscles (biceps muscle, gastrocnemius muscle and tibialis anterior muscle) were also imaged in five more healthy adults increasing the total number of images to 25. The images of the two tendons were collected with the ankle and knee joints placed at 90 deg. The Achilles tendon's insertion into the calcaneus or the patellar tendon's insertion into the tibia respectively was identified first and then axial images were recorded as the probe was moved in the proximal direction. In both cases ultrasound imaging was performed using a linear probe (L12-5L40S-3 5-12 MHz 40 mm, MicrUs EXT-1H Telemed UAB, Vilnius, Lithuania) and a stand-off (Sonokit, Sonogel, Vertriebs, Gmbh, Sonic velocity 1405 m/s, absorption 0.09 dB/MHz.mm and reflection: 2.4 %) to improve docking between transducer and skin. Muscles were imaged both in the axial and longitudinal planes using a different linear probe (L18−5 18−5 MHz, Phillips Epiq).

During the analysis of these images, the initial contour for segmentation was chosen to be a circle with radius (r) [7]. As a result, five hyperparameters ($\rho, \gamma, \beta_1, \beta_2$ and r) in total had to be defined to run the segmentation process. The values of some of these hyperparameters were defined based on literature (γ, β_1, β_2) while others (ρ, r) were defined to produce a satisfactory delineated output for GD; namely a delineated output that contains at least 80 % of the sub regions in the input image. The same values were used for both the models and for all GD variants.

According to literature, the fitting terms were both set equal to one ($\beta_1 = \beta_2 = 1$) and the area constraint was ignored (i.e.) $\gamma = 0$ [7]. Parameter ρ was set to 0.0009 through a trial-and-error approach to provide a satisfactory delineated output. Parameter ρ should be relatively small when the segmentation process targets individual small structures, and it should be relatively large when larger structures or clusters of structure are to be detected. Even though changes in the value of ρ affect the delineated output, the relative computational efficiency of GD and its variants is not expected to be affected.

The initial circle radius (r) was the only parameter that was set separately for each individual image based on the following sequence of steps:

Step 1: Read the input image and perform convolution operation between the input image and the Laplacian kernel $\begin{bmatrix} 0 & 1 & 0 \\ 1 & -4 & 1 \\ 0 & 1 & 0 \end{bmatrix}$ (i.e.) $T \longleftarrow z \star \mathscr{L}$ where z denotes input image; $\star$ denotes convolution operation; $\mathscr{L}$ denotes Laplacian kernel and T denotes output image

Step 2: In T, set the first row, first column, last row and last column to zero. Let this image be T_0

Step 3: Find the maximum value of absolute value of each column of the matrix T_0. Form a row vector ($\overrightarrow{R_1}$) that contains the maximum value of absolute value of each of the columns of the matrix T_0.

$\overrightarrow{R_1} \longleftarrow [\max(|c_1|), \max(|c_2|), \max(|c_3|), \ldots\ldots \max(|c_n|)]$; $\overrightarrow{R_1}$ denotes row vector; $c_1, c_2 \ldots c_n$ denotes the 1st, 2nd…. n^{th} column respectively of matrix T_0

Step 4: Find a threshold value. Threshold value $t = \max(\overrightarrow{R_1}) \times 0.5$

Step 5: Form a matrix Y with absolute values of T_0 that are greater than t (i.e.) $Y \longleftarrow |T_0| > t$

Step 6: $\overrightarrow{idx} \longleftarrow \begin{bmatrix} l_1 \\ l_2 \\ \vdots \\ l_j \end{bmatrix}$ where $l_1, l_2 \ldots l_j$ are linear indices of Y; $\overrightarrow{idx}$ denotes vector

Step 7: Convert the linear index vector $\overrightarrow{idx}$ into row column indices of a matrix that is of size of T_0. Let *row*=row indices of the matrix and *column* = column indices of the matrix

Step 8: $c_x \longleftarrow mean(row)$ *and* $c_y \longleftarrow mean(column)$

Step 9: Radius of the circle $(r) \longleftarrow \max\left(\frac{2}{3} \times r_1, r_{max}\right)$; $r_1 \longleftarrow \min\left((\min(c_x, p - c_x), (\min(c_y, q - c_y)\right)$; p = number of rows in z ; q = number of columns in z ; r_{max} is varied between 50 and 150 pixels in steps of 50 pixels and the input image is processed using CV model with GD. The value of r_{max} for which the delineated output contains at least 80 % of the sub regions in the input image is used to calculate r according to step 9 (Table 2).

In the case of GD, PGD and NA-GD optimization techniques, a fixed value of step size (ξ) also had to be defined. Choosing a relatively small step size unnecessarily slows down convergence while a relatively large step size could result in overshooting the optimum solution and cause problems with convergence. With this in mind, step size was optimised for GD (optimum $\xi = 0.51$) and the same value was then used for PGD and NA-GD.

The performance of the five proposed variants of GD (NA-GD, BB-GD, hybrid, PGD, BB-PGD) was assessed with regards to their average processing time (in seconds) and average number of iterations to convergence. Furthermore, to test whether the use of the proposed variants of GD had a significant effect on the segmentation output, the similarity between the output of GD (reference) and the proposed variants of GD was also assessed. More specifically, the similarity between the reference and the delineated output obtained by using each proposed GD variant was quantified using the structural similarity index (SSIM) and correlation coefficient (CC). CC is a metric that calculates the probability that a linear relationship exists between a reference image and a test image. Similarly, SSIM is a metric that reflects the degree of structural similarity between a test image and a reference image [39–45]. It is meaningful to compute SSIM only if correlation exists between the reference image and the test image and the degree of correlation should be at least 0.5 [46].

An optimization technique that speeds up the convergence process

Table 2
The average(±std.dev.) of the radius of the initial circle for segmentation (r) that was used for each tissue. Std.dev. = 0 when the same value was used for all five images.

Anatomical region	Number of images	Average radius of the initial contour (r_{avg}) in pixels
Achilles tendon	5	80 (±0)
Patellar tendon	5	150 (±0)
Biceps muscle	5	58 (±10)
Gastrocnemius muscle	5	72 (±21)
Tibialis anterior muscle	5	92 (±40)

without significantly changing the delineated output relative to GD is considered to be the most appropriate one. Optimum SSIM indicates least structural distortion (relative to reference) among the proposed variants of GD. In this case study, optimum refers to the greatest value among the available SSIM scores. Therefore, an optimization technique that gives an average CC of at least 0.5 together with the maximum average SSIM and a substantial reduction in computational cost will be considered as the most suitable optimization technique for processing US image of musculoskeletal tissues.

All the US images analyzed in this study and a detailed list of hyperparameters used for each one them can be found in Supplementary material B.

3. Results

The overall average(±std.dev.) of processing time of the conventional CV model with GD for all 25 musculoskeletal US images was 125 s (±65 s), while solution was completed after 4735(±2380) iterations. The convergence of level set to steady state was substantially sped up by all proposed variants of GD (Fig. 1). When the achieved reduction in processing time was calculated separately for each individual image, it was found that on average, the NA-GD, BB-GD and hybrid method reduced processing time by 96.43 %(±1.56 %), 97.57 % (±1.04 %) and 97.61 %(±1.02 %) respectively. A slightly lower reduction was achieved by BB-PGD (87.84 %(±5.20 %)) and a significantly lower reduction by PGD (5.14 %(±37.91 %)). This significant reduction in average processing time was achieved due to a substantial decrease in the average number of iterations taken for convergence of level set to steady state (Fig. 2).

The average processing time and average number of iterations taken for processing the same musculoskeletal US images with the MCV model was significantly increased relative to the conventional CV model when the reference optimization technique (i.e.GD) was used. However, when the proposed variants of GD were used, the average processing time and average number of iterations dropped to the same level as for the CV model (Figs. 1 and 2). More specifically, the average(±std.dev.) processing time and average(±std.dev.) number of iterations taken for MCV model with GD were 1011s(±1181s) and 36,152(±37,838) respectively. Similar to before, the NA-GD, BB-GD and the hybrid methods achieved the highest reduction in average processing time (Fig. 1). On average, the processing time for each image was reduced by 98.89 %(±0.94 %), 99.25 % (±0.77 %) and 99.23 %(±0.65 %) respectively. A slightly lower reduction was achieved by BB-PGD (95.82 %(±3.60 %)) and a significantly lower reduction was achieved by PGD (75.35 %(±18.46 %)). The average number of iterations was reduced between 99.61 %(±0.32 %) and 99.96 %(±0.04 %) by the proposed variants of GD in the case of the MCV model.

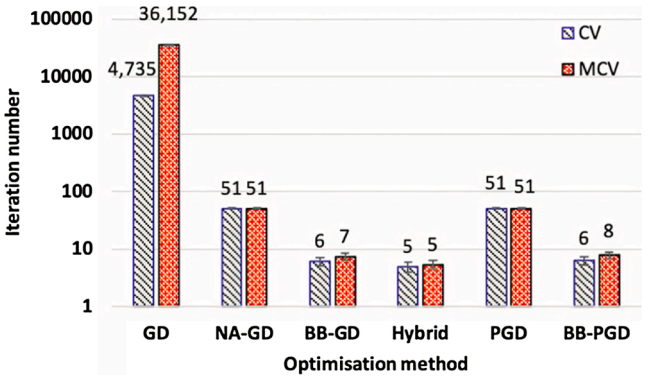

Fig. 2. The average number of iterations that were needed to complete the segmentation process by the conventional CV and MCV model and different optimization methods. The exact average number of iterations is also shown for each case.

Least structural distortion relative to GD can be inferred from the greatest average SSIM. From Fig. 3, out of all proposed variants of GD, it is evident that the combination of the MCV model with the BB-PGD optimization method has the greatest average SSIM (0.91 ± 0.06). Though, in this case, BB-PGD achieved the fourth best reduction in average processing time (95.82 %±3.60 %), it appears to be the best combination for processing US images of musculoskeletal tissues. Typical delineation results obtained by processing each musculoskeletal tissue under study with the MCV model and BB-PGD are shown in Fig. 4. The same optimization method was found to be the best for the conventional CV too. However, in that case, the achieved average SSIM score was relatively lower (0.81 ± 0.06). In all cases, CC was higher than 0.5.

4. Discussion

The CV model and its speckle noise handling variant called MCV model were considered in this study. The difference between the two models is that MCV includes a physical modelling of speckle noise. Since speckle noise is the predominant type of noise in US imaging, MCV can be more robust to noise and, therefore, better suited for analysing US images.

Though CV and MCV models are topologically flexible, less sensitive to noise and initial position of the shape model and can segment structures with weak boundaries, a key limitation of these models is their computational inefficiency. The factors that hamper the computational efficiency of aforementioned models are the use of GD to solve the non-convex optimization problem of the CV and MCV models and the use of

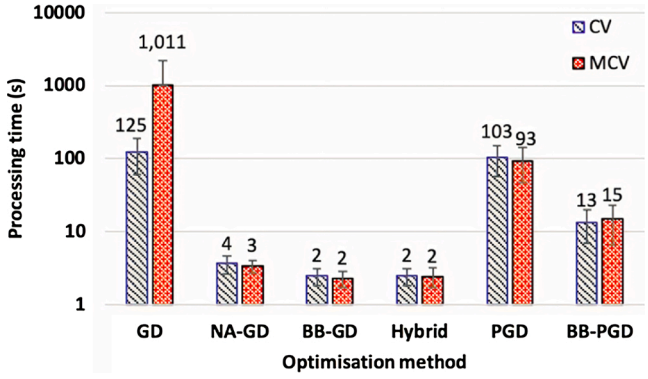

Fig. 1. The average processing time taken for segmenting musculoskeletal US images with the conventional CV and MCV model and different optimization methods. The exact value of average processing time is also shown for each case.

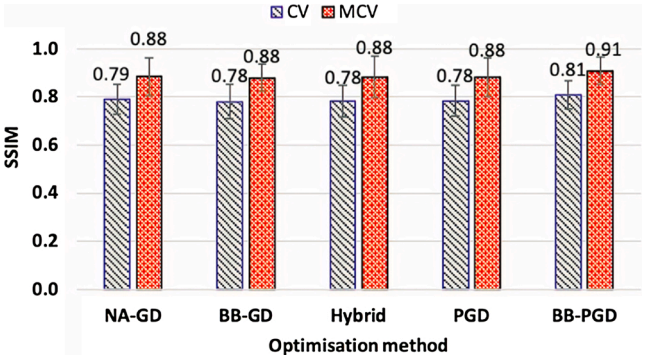

Fig. 3. Assessment of the similarity between the delineated output of GD and of its proposed variants for the CV and MCV models. Similarity is assessed with the help of the structural similarity index (SSIM). SSIM takes values between 1 (perfect similarity) and 0(no similarity at all).

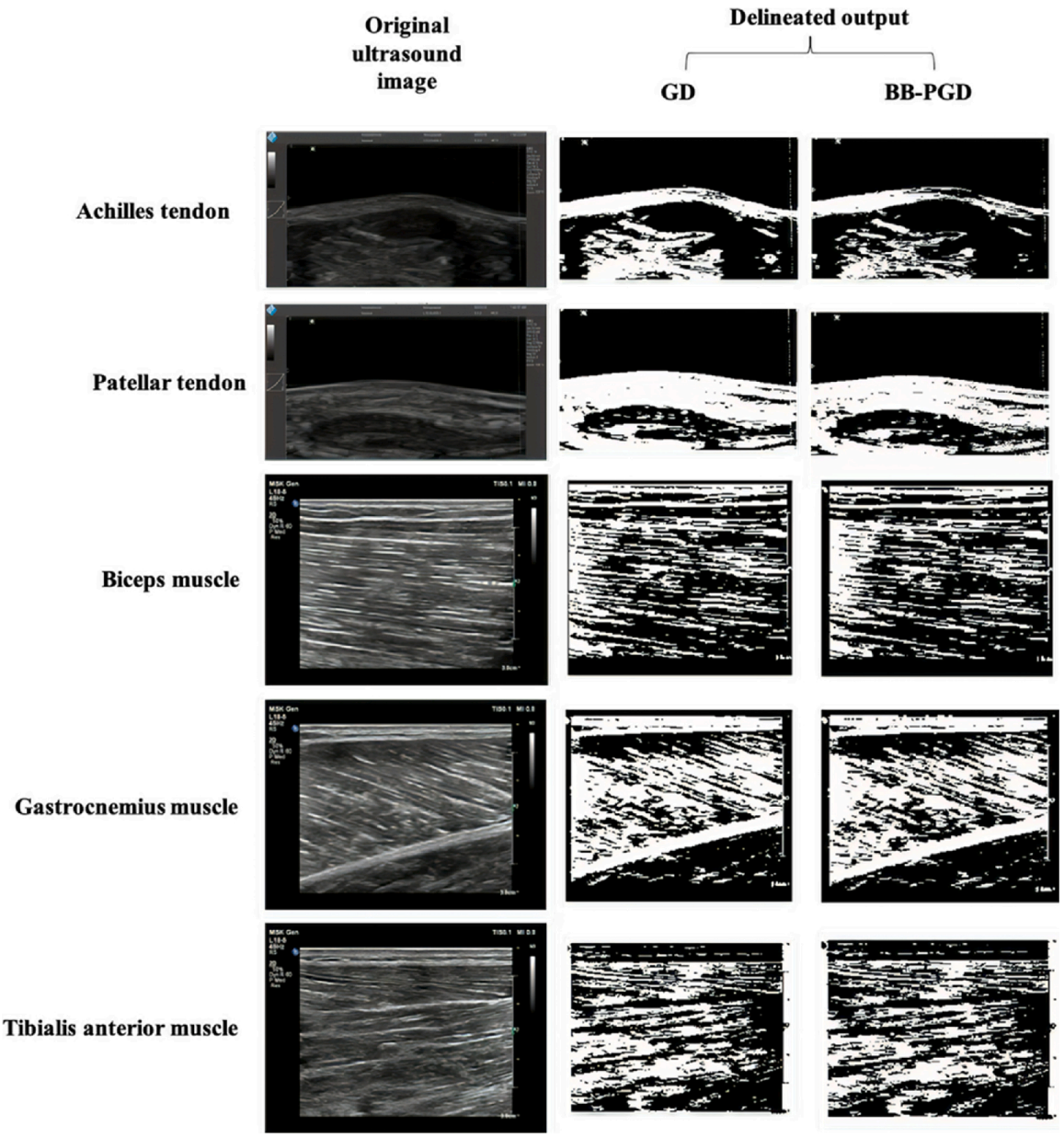

Fig. 4. Comparison between the delineated outputs of GD and BB-PGD optimization methods. Typical images from all five anatomical are presented.

numerical remedies to maintain the constraint on LSF during its evolution. In this context, the purpose of this study was to test whether alternative first order optimization schemes could improve the computational efficiency of the CV and MCV models.

Three optimization techniques were proposed to overcome the numerical difficulties encountered while solving a non-convex optimization problem with GD (convergence towards local optima and slow convergence towards global optimum). Two variants of GD from literature (NA-GD, BB-GD) and a newly developed hybrid method were proposed to address this issue. A fourth variant of GD from literature (PGD) was proposed to address the limitation associated with level set modelling of evolving boundaries which also can compromise the computational efficiency of the segmentation process. A fifth and final GD variant was developed here to try to address both aforementioned problems at the same time (BB-PGD).

For both models (i.e. CV and MCV), the BB-GD and hybrid optimization methods achieved the maximum reduction in computational time and appear to be the most computationally efficient ones (Fig. 1). At the same time, however, these methods also appear to affect the final delimited output. This is evident by the relatively low SSIM against the output of GD (i.e. against reference).

When SSIM is taken into consideration, then the BB-PGD method emerges as the most appropriate one. More specifically, BB-PGD reduced the processing time by 87.84 %(±5.20 %) and 95.82 %(±3.60 %) for the CV and MCV models respectively, while achieving the minimum changes in the delineated output (SSIM scores of 0.81 ± 0.06 and 0.91 ± 0.06 respectively).

Previous theoretical work has established that the BB-GD method converges globally both for bounded constrained and non-convex optimization problems [47]. A similar proof for the BB-PGD is not available [28]. Having said that, BB-PGD appears to be well suited for the specific application presented in this study. This is evident by the improved SSIM score relative to BB-GD. However, in the absence of a theoretical proof of global convergence, the validity of BB-PGD will have to be established on an application-specific basis.

The existing approaches for delineation of target structures from an US video are either model based or tracking based. The most representative model based and tracking based approaches are the snake contour

and Kalman filter respectively [48].Kalman filter and its variants (Extended and unscented Kalman filter) has the ability to track the substantial variation in the shape of boundary of target structures between the frames [48–50]. However, the limitation of Kalman filter approach is that tracking fails when there is an irregular variation in boundary of the target structures between frames. On the other hand, snake contour has the ability to segment the irregular variation in shape of the boundary more accurately than the Kalman filter. However, since snake contour doesn't have prior knowledge on interframe shape variations of the target structures, it fails to accurately detect boundaries when there is a substantial movement or change in size of the target structures between frames [48,51]. Moreover, the inherent limitations of US images with respect to low contrast and image quality interferes with the performance of snake model since the external energy that pulls the initial contour towards the structure of interest is formed by gradient information. The gradient may not be well defined in the areas of low contrast and when the image is noisy. In addition, in the classical snake model, in order to get a satisfactory segmentation result, the initial contour should be placed close to the structures of interest. The solutions proposed in the literature to address the initialization sensitivity problem are based on different choice of external energy such as multiscale Gaussian potential force, balloon force, distance potential force and gradient vector flow [3,52–54].The base idea behind these proposed solutions is to modify the external energy so that the capture range of the snake model is increased thereby circumventing the need to place the initial contour very close to the target structure. However, the snake model and its variants cannot delineate multiple target structures simultaneously due to its topological rigidity [2].CV model is the solution proposed in the literature to handle the aforementioned limitations of snake model [2,53].The CV model is topologically flexible, less sensitive to noise and to the initial position of the shape model and can reliably segment structures with weak boundaries [3,8,9,52,53].

Deep learning-based approaches have also been successfully used in the analysis of US images and appear to offer promising possibilities for enhancing clinical research and diagnostic US [55]. At the same time, however, their use is also restricted by two key limitations: a) the accuracy of delineation depends strongly on the quality of the training dataset and b) they are computationally expensive [56–60]. On the other hand, deformable models do not require any training to learn about the shapes of structures of interest and constraints since these models delineate the structures of interest by minimization of an energy functional. In general, deformable model-based segmentation is also very computational expensive. However, the method proposed in the present study overcomes this limitation to open the way for its use in applications where noise-robust real-time delineation is needed (e.g. during US-guided interventions).

To the authors' knowledge, the present study is the first to demonstrate that the computational efficiency of deformable models can be substantially improved by using alternative first order optimization techniques. To this end, projection based first order optimization techniques from the literature (PGD, BB-PGD) were used for the first time in conjunction with the CV model. A new hybrid optimization method which combines the advantages of NA-GD and BB-GD was also developed and tested.

Even though this study focused on musculoskeletal images, the findings and proposed method for improving the computational efficiency of deformable model-based segmentation are transferable to the imaging of other anatomical areas too. Computerized delineation of structures of interest from US images can play a vital role in numerous clinical applications such as the quantification of tissue volume and the localization of pathological areas. However, in the vast majority of envisaged applications of computerized delineation, the assumption is that US images will be recorded first and then analysed which eliminates the possibility of real-time delineation [56,57,59,60].On the contrary, the substantial reduction in processing time that was achieved by the proposed optimization schemes can open the way for applications where US images are continuously analysed and displayed in real-time on the US unit's screen. Being able to overlay a noise-robust sharp delineated image onto the conventional B-mode US image could provide clinicians working with US with an alternative way of viewing US to enhance and complement their work. This capability could be particularly useful to enhance US-guided interventions.

At this point, it needs to be highlighted that the purpose of this study was to prove whether the computational efficiency of CV and MCV models could be substantially improved by using alternative first order optimization schemes. Further studies involving a greater number of images from more anatomical areas will be needed to identify and validate the most appropriate optimization method for the CV and MCV models.

Contribution by authors

Saru Meena Ramu developed the theoretical framework of the presented idea and derived the mathematical model. All the authors were involved into the planning and implementation of the numerical simulations. Kannan Krithivasan verified the correctness of the derived mathematical model and optimization techniques. Panagiotis Chatzistergos and Nachiappan Chockalingam collected the original ultrasound images of musculoskeletal tissues that were used in the present study. Saru Meena Ramu and Jaikanth Jayakumar together carried out the numerical simulations. The results obtained from the numerical simulations were analysed by Saru Meena Ramu. Analysis on the results obtained and the inferences drawn from the analysis were critically evaluated by Panagiotis Chatzistergos and they were mathematically evaluated by Kannan Krithivasan. Saru Meena Ramu wrote the manuscript and revising the manuscript critically for important intellectual content was done together by Panagiotis Chatzistergos and Saru Meena Ramu. Muthaiah Rajappa supervised the work. Funding acquisition was done together by Panagiotis Chatzistergos, Nachiappan Chockalingam and Muthaiah Rajappa. All authors provided a critical feedback and helped to shape the research, analysis and manuscript.

Funding

This work was supported by the UK-India Education and Research Initiative (UKIERI) grant 'Ultrasound based assessment of tissue biomechanics to enhance the clinical management of foot related pathologies' (Project reference number: DST/INT/UK/P-145/2016). Financial support was also obtained from Department of Science and Technology (DST), New Delhi. The authors would also like to thank TATA Realty-IT City - SASTRA Srinivasa Ramanujam Research cell of SASTRA university.

Availability of data and material

All the images that were used in this study can be found in Supplementary material B.

Code availability

Available upon request.

Declaration of Competing Interest

The authors declare that they have no known competing financial interests or personal relationships that could have appeared to influence the work reported in this paper.

Appendix A. Supplementary data

Supplementary material related to this article can be found, in the online version, at https://doi.org/10.1016/j.bspc.2021.102560.

References

[1] S. Dahdouh, E.D. Angelini, G. Grange, I. Bloch, Segmentation of embryonic and fetal 3D ultrasound images based on pixel intensity distributions and shape priors, Med. Image Anal. 24 (2015) 255–268, https://doi.org/10.1016/j.media.2014.12.005.

[2] J.S. Suri, A.A. Farag, Deformable Models Theory and Biomaterial Applications, 2007, https://doi.org/10.1007/978-0-387-68343-0.

[3] I.N. Bankman, Handbook of Medical Image Processing and Analysis, Elsevier Inc., 2009, https://doi.org/10.1016/B978-0-12-373904-9.X0001-4.

[4] T. Albrecht, M. Lüthi, T. Vetter, Deformable Models, in: S.Z. Li, A. Jain (Eds.), Encyclopedia of Biometrics, Springer US, Boston, MA, 2009, pp. 210–215, https://doi.org/10.1007/978-0-387-73003-5_88.

[5] Y. Yuan, C. He, Adaptive active contours without edges, Math. Comput. Model. 55 (2012) 1705–1721, https://doi.org/10.1016/j.mcm.2011.11.014.

[6] Y. Chen, X. Yue, R.Y.D. Xu, H. Fujita, Region scalable active contour model with global constraint, Knowledge Based Syst. 120 (2017) 57–73, https://doi.org/10.1016/j.knosys.2016.12.023.

[7] T.F. Chan, L.A. Vese, Active contours without edges, IEEE Trans. Image Process. 10 (2001) 266–277, https://doi.org/10.1109/83.902291.

[8] J. Spencer, Variational Methods for Image Segmentation (Doctoral Dissertation), University of Liverpool, Liverpool, United Kingdom, 2016.

[9] C.P. Lee, Robust Image Segmentation Using Active Contours: Level Set Approaches (Doctoral Dissertation), North Carolina State University, Raleigh,North Carolina, United States, 2005.

[10] X.-F. Wang, D.-S. Huang, H. Xu, An efficient local Chan-Vese model for image segmentation, Pattern Recognit. 43 (2010) 603–618, https://doi.org/10.1016/j.patcog.2009.08.002.

[11] J. Duan, Z. Pan, X. Yin, W. Wei, G. Wang, Some fast projection methods based on Chan-Vese model for image segmentation, EURASIP J. Image Video Process. 2014 (2014) 7, https://doi.org/10.1186/1687-5281-2014-7.

[12] T. Andersson, G. Läthén, R. Lenz, M. Borga, Modified gradient search for level set based image segmentation, IEEE Trans. Image Process. 22 (2013) 621–630, https://doi.org/10.1109/TIP.2012.2220148.

[13] E.S. Brown, T.F. Chan, X. Bresson, Completely convex formulation of the Chan-Vese image segmentation model, Int. J. Comput. Vis. 98 (2012) 103–121, https://doi.org/10.1007/s11263-011-0499-y.

[14] R. Chan, A. Lanza, S. Morigi, F. Sgallari, Convex non-convex image segmentation, Numer. Math. 138 (2018) 635–680, https://doi.org/10.1007/s00211-017-0916-4.

[15] K. Saini, M.L. Dewal, M. Rohit, A fast region-based active contour model for boundary detection of echocardiographic images, J. Digit. Imaging 25 (2012) 271–278, https://doi.org/10.1007/s10278-011-9408-8.

[16] Y. Yang, B. Wu, Split Bregman method for minimization of improved active contour model combining local and global information dynamically, J. Math. Anal. Appl. 389 (2012) 351–366, https://doi.org/10.1016/j.jmaa.2011.11.073.

[17] T. Goldstein, X. Bresson, S. Osher, Geometric applications of the split bregman method: segmentation and surface reconstruction, J. Sci. Comput. 45 (2010) 272–293, https://doi.org/10.1007/s10915-009-9331-z.

[18] Y. Yang, C. Li, C.-Y. Kao, S. Osher, Split bregman method for minimization of region-scalable fitting energy for image segmentation, in: G. Bebis, R. Boyle, B. Parvin, D. Koracin, R. Chung, R. Hammound, M. Hussain, T. Kar-Han, R. Crawfis, D. Thalmann, D. Kao, L. Avila (Eds.), Advances in Visual Computing, Springer, Berlin Heidelberg, Berlin, Heidelberg, 2010, pp. 117–128.

[19] J. Nocedal, S. Wright, Numerical Optimization, 2006, https://doi.org/10.1007/978-0-387-40065-5.

[20] C. Jin, P. Netrapalli, M.I. Jordan, Accelerated Gradient Descent Escapes Saddle Points Faster Than Gradient Descent, 2017.

[21] J. Barzilai, J.M. Borwein, Two-point step size gradient methods, IMA J. Numer. Anal. 8 (1988) 141–148, https://doi.org/10.1093/imanum/8.1.141.

[22] Y. Sun, Notes on first-order methods for minimizing smooth functions. MS&E 318: Large-Scale Numerical Optimization, 2015.

[23] V. Estellers, Geometric Variational Models for Inverse Problems in Imaging (Doctoral dissertation), École polytechnique fédérale de Lausanne, Lausanne, Switzerland, 2013.

[24] C. Li, C. Xu, C. Gui, M.D. Fox, Distance regularized level set evolution and its application to image segmentation, IEEE Trans. Image Process. 19 (2010) 3243–3254, https://doi.org/10.1109/TIP.2010.2069690.

[25] C.Y. Yu, W.S. Zhang, Y.Y. Yu, Y. Li, A novel active contour model for image segmentation using distance regularization term, Comput. Math. With Appl. 65 (2013) 1746–1759, https://doi.org/10.1016/j.camwa.2013.03.021.

[26] Chunming Li, Chenyang Xu, Changfeng Gui, M.D. Fox, Level set evolution without re-initialization: a new variational formulation, in: 2005 IEEE Computer Society Conference on Computer Vision and Pattern Recognition (CVPR'05), vol. 1, 2005, pp. 430–436, https://doi.org/10.1109/CVPR.2005.213.

[27] P. Jain, P. Kar, Non-convex optimization for machine learning, Found. Trends Mach. Learn. 10 (2017) 142–336, https://doi.org/10.1561/2200000058.

[28] Y.-H. Dai, R. Fletcher, Projected Barzilai-Borwein methods for large-scale box-constrained quadratic programming, Numer. Math. 100 (2005) 21–47, https://doi.org/10.1007/s00211-004-0569-y.

[29] D. Tenbrinck, X. Jiang, Image segmentation with physical noise models. Biomedical Image Segmentation Advances and Trends, 1st ed., CRC Press, 2016, pp. 461–484, https://doi.org/10.1201/9781315372273.

[30] K. Krissian, R. Kikinis, C.-F. Westin, K. Vosburgh, Speckle-constrained filtering of ultrasound images, Proceedings of the IEEE Computer Society Conference on Computer Vision and Pattern Recognition (2005) 547–552, https://doi.org/10.1109/CVPR.2005.331.

[31] T. Loupas, Digital Image Processing for Noise Reduction in Medical Ultrasonics (Doctoral Dissertation), University of Edinburgh, Edinburgh,United Kingdom, 1988.

[32] D. Tenbrinck, X. Jiang, Image segmentation with arbitrary noise models by solving minimal surface problems, Pattern Recognit. 48 (2015) 3293–3309, https://doi.org/10.1016/j.patcog.2015.01.006.

[33] G. Wang, Q. Dong, Z. Pan, X. Zhao, J. Yang, C. Liu, Active contour model for ultrasound images with Rayleigh distribution, Math. Probl. Eng. 2014 (2014), https://doi.org/10.1155/2014/295320.

[34] D. Tenbrinck, A. Sawatzky, X. Jiang, M. Burger, W. Haffner, P. Willems, M. Paul, J. Stypmann, Impact of physical noise modeling on image segmentation in echocardiography, in: Eurographics Workshop on Visual Computing for Biology and Medicine, 2012, 2012, pp. 33–40.

[35] S. Becker, Y. Lecun, Improving the Convergence of Back-propagation Learning With Second-order Methods, 1989.

[36] D. Mandal, A. Chatterjee, M. Maitra, Improved Chan-Vese Image Segmentation Model Using Delta-Bar-Delta Algorithm, Springer, Cham, 2014, pp. 267–274, https://doi.org/10.1007/978-3-319-07353-8_32.

[37] T. Andersson, G. Läthén, R. Lenz, M. Borga, A fast optimization method for level set segmentation, in: A.-B. Salberg, J.Y. Hardeberg, R. Jenssen (Eds.), Image Analysis, Springer Berlin Heidelberg, Berlin, Heidelberg, 2009, pp. 400–409.

[38] M. Schmidt, Rates of Convergence, 2017. https://www.cs.ubc.ca/~schmidtm/Courses/540-W18/L5.pdf.

[39] A. Geurts, G. Sakas, A. Kuijper, M. Becker, T. von Landesberger, Visual comparison of 3D medical image segmentation algorithms based on statistical shape models. Lecture Notes in Computer Science (Including Subseries Lecture Notes in Artificial Intelligence and Lecture Notes in Bioinformatics), Springer Verlag, 2015, pp. 336–344, https://doi.org/10.1007/978-3-319-21070-4_34.

[40] V. Yeghiazaryan, I. Voiculescu, An Overview of Current Evaluation Methods Used in Medical Image Segmentation, 2015.

[41] Z. Wang, A.C. Bovik, E.P. Simoncelli, 8.3 Structural Approaches to Image Quality Assessment, Academic Press, 2005.

[42] G. Palubinskas, Image similarity/distance measures: what is really behind MSE and SSIM? Int. J. Image Data Fusion 8 (2017) 32–53, https://doi.org/10.1080/19479832.2016.1273259.

[43] Z. Wang, A.C. Bovik, Mean squared error : love it or leave it? IEEE Signal Process. Mag. 26 (2009) 98–117, https://doi.org/10.1109/MSP.2008.930649.

[44] K. Seshadrinathan, T.N. Pappas, R.J. Safranek, J. Chen, Z. Wang, H.R. Sheikh, A. C. Bovik, Image Quality Assessment, 1st ed., Elsevier, 2009 https://doi.org/10.1016/B978-0-12-374457-9.00021-4.

[45] P. Ndajah, H. Kikuchi, M. Yukawa, H. Watanabe, S. Muramatsu, SSIM Image Quality Metric for Denoised Images, 2010.

[46] P. Schober, L.A. Schwarte, Correlation coefficients: appropriate use and interpretation, Anesth. Analg. 126 (2018) 1763–1768, https://doi.org/10.1213/ANE.0000000000002864.

[47] Y. Xiao, H. Song, Z. Wang, A modified conjugate gradient algorithm with cyclic Barzilai–Borwein steplength for unconstrained optimization, J. Comput. Appl. Math. 236 (2012) 3101–3110, https://doi.org/10.1016/j.cam.2012.01.032.

[48] S.-H. Lee, S. Lee, Adaptive Kalman snake for semi-autonomous 3D vessel tracking, Comput. Methods Programs Biomed. 122 (2015) 56–75, https://doi.org/10.1016/j.cmpb.2015.06.008.

[49] S.-H. Lee, S. Lee, Unscented kalman snake for 3D vessel tracking, J. Int. Soc. Simul. Surg. 2 (2015) 17–25, https://doi.org/10.18204/JISSiS.2015.2.1.017.

[50] Z. Gao, Y. Li, Y. Sun, J. Yang, H. Xiong, H. Zhang, X. Liu, W. Wu, D. Liang, S. Li, Motion tracking of the carotid artery wall from ultrasound image sequences: a nonlinear state-space approach, IEEE Trans. Med. Imaging 37 (2018) 273–283, https://doi.org/10.1109/TMI.2017.2746879.

[51] S. Zhao, Z. Gao, H. Zhang, Y. Xie, J. Luo, D. Ghista, Z. Wei, X. Bi, H. Xiong, C. Xu, S. Li, Robust segmentation of intima–Media borders with different morphologies and dynamics during the cardiac cycle, IEEE J. Biomed. Health Inform. 22 (2018) 1571–1582, https://doi.org/10.1109/JBHI.2017.2776246.

[52] T. McInerney, D. Terzopoulos, Deformable models in medical image analysis: a survey, Med. Image Anal. 1 (1996) 91–108, https://doi.org/10.1016/S1361-8415(96)80007-7.

[53] R. Hegadi, A. Kop, M. Hangarge, A survey on deformable model and its applications to medical imaging, Int. J. Comp. Appl. RTIPPR (2010) 64–75.

[54] Z. Zhang, C. Duan, T. Lin, S. Zhou, Y. Wang, X. Gao, GVFOM: a novel external force for active contour based image segmentation, Inf. Sci. 506 (2019), https://doi.org/10.1016/j.ins.2019.08.003.

[55] S. Liu, Y. Wang, X. Yang, B. Lei, L. Liu, S.X. Li, D. Ni, T. Wang, Deep learning in medical ultrasound analysis: a review, Engineering 5 (2019) 261–275, https://doi.org/10.1016/j.eng.2018.11.020.

[56] D.L. Pham, J.L. Prince, A survey of current methods in medical image segmentation, IEEE Trans. Med. Imaging 18 (1999) 737–752.

[57] A. Mansoor, U. Bagci, B. Foster, Z. Xu, G.Z. Papadakis, L.R. Folio, J.K. Udupa, D. J. Mollura, Segmentation and image analysis of abnormal lungs at CT: current approaches, challenges, and future trends, RadioGraphics. 35 (2015) 1056–1076, https://doi.org/10.1148/rg.2015140232.

[58] T. Hoang Ngan Le, K. Luu, C.N. Duong, K.G. Quach, T.D. Truong, K. Sadler, M. Savvides, Active contour model in deep learning era: a revise and review, in: D. Oliva, S. Hinojosa (Eds.), Applications of Hybrid Metaheuristic Algorithms for

Image Processing, Springer International Publishing, Cham, 2020, pp. 231–260, https://doi.org/10.1007/978-3-030-40977-7_11.

[59] W. Wang, Y. Wang, Y. Wu, T. Lin, S. Li, B. Chen, Quantification of full left ventricular metrics via deep regression learning with contour-guidance, IEEE Access 7 (2019) 47918–47928, https://doi.org/10.1109/ACCESS.2019.2907564.

[60] W. Shen, W. Xu, H. Zhang, Z. Sun, J. Ma, X. Ma, S. Zhou, S. Guo, Y. Wang, Automatic segmentation of the femur and tibia bones from X-ray images based on pure dilated residual U-Net, Inverse Probl. Imaging (2020) 1–15, https://doi.org/10.3934/ipi.2020057.